



CrossMark
click for updates

Cite this: *Lab Chip*, 2016, 16, 532

Continuous inertial microparticle and blood cell separation in straight channels with local microstructures†

Zhenlong Wu,^{ab} Yu Chen,^{‡c} Moran Wang^c and Aram J. Chung^{*a}

Fluid inertia which has conventionally been neglected in microfluidics has been gaining much attention for particle and cell manipulation because inertia-based methods inherently provide simple, passive, precise and high-throughput characteristics. Particularly, the inertial approach has been applied to blood separation for various biomedical research studies mainly using spiral microchannels. For higher throughput, parallelization is essential; however, it is difficult to realize using spiral channels because of their large two dimensional layouts. In this work, we present a novel inertial platform for continuous sheathless particle and blood cell separation in straight microchannels containing microstructures. Microstructures within straight channels exert secondary flows to manipulate particle positions similar to Dean flow in curved channels but with higher controllability. Through a balance between inertial lift force and microstructure-induced secondary flow, we deterministically position microspheres and cells based on their sizes to be separated downstream. Using our inertial platform, we successfully sorted microparticles and fractionized blood cells with high separation efficiencies, high purities and high throughputs. The inertial separation platform developed here can be operated to process diluted blood with a throughput of 10.8 mL min⁻¹ via radially arrayed single channels with one inlet and two rings of outlets.

Received 23rd November 2015,
Accepted 10th December 2015

DOI: 10.1039/c5lc01435b

www.rsc.org/loc

Introduction

Blood cell separation is an essential and critical step in clinical diagnosis, therapeutic methods and cell biology because each blood component reveals important health information.^{1–5} For example, changes in erythrocyte or red blood cell (RBC) levels and morphologies have been used to diagnose blood diseases such as hemolysis, malaria and anemia.^{1,3} Leukocytes, or white blood cells (WBCs), are useful indicators of immune system functions, mediating the immune response to various pathogens.⁶ Abnormal levels or deformations of

WBCs are closely related to immune disorder, infection or blood cancer.³ In order to obtain each blood type for the aforementioned purposes, various methods are conducted in laboratories,¹ and there are two conventional methods for blood cell separation: flow cytometry and centrifugation. Fluorescence-activated cell sorting (FACS) is a representative flow cytometric approach to classify heterogeneous cell samples. While the technique offers an effective high-throughput separation, a time and effort consuming fluorescent labelling process is required which could potentially alter the intrinsic cell properties⁷ and lead to irreversible cell damage.⁸ Moreover, the system requires costly instrumentation, skilled operators and multiple passes for full analysis.^{9,10} As another drawback, significantly high volumes of logistically burdensome sheath fluids are necessary for the cell focusing step. Alternatively, blood cells can be separated using a centrifugation process widely used in the laboratory. The process itself is straightforward, though to precisely fractionize blood components, trained technicians should carry out the process. In addition, the process normally includes a RBC lysis step which potentially alters cell properties.¹¹

New technologies based on microfluidics have attracted considerable attention for blood cell separation due to a number of inherent opportunities over the aforementioned conventional technologies.² Microfluidic approaches can deliver high purity, high efficiency, high-throughput, simple

^a Department of Mechanical, Aerospace, and Nuclear Engineering, Rensselaer Polytechnic Institute (RPI), 110 8th Street, Troy, NY 12180, USA.

E-mail: chungaj6@rpi.edu

^b School of Aeronautic Science and Engineering, Beihang University, Beijing 100191, China

^c Department of Engineering Mechanics, School of Aerospace, Tsinghua University, Beijing 100084, China

† Electronic supplementary information (ESI) available: Five movies are included as part of this work. Movie S1 shows the experimental separation of 5.5 and 9.9 μm polystyrene microspheres. Movies S2 and S3 illustrate numerical analysis of single-sized particle migration (5.5 and 9.9 μm polystyrene beads), and Movie S4 shows numerical predictions of 5.5 and 9.9 μm polystyrene bead mixture separation. Movie S5 demonstrates the separation of RBCs and WBCs from 0.5% (v/v) diluted human blood. See DOI: 10.1039/c5lc01435b

‡ Present address: Department of Civil and Environmental Engineering, University of Illinois at Urbana-Champaign, Urbana, IL 61801, USA.

and low-cost features.^{12–14} Within microfluidic devices, blood cells can be classified by applying external acoustic,^{15,16} optical,¹⁷ and electric^{18,19} forces. Microfluidic coupling with external forces can actively manipulate and control cell positions with great precision; however, the systems are relatively complex with limited throughput, making them unattractive for blood cell separation. On the other hand, passive (*i.e.*, hydrodynamic) methods such as hydrodynamic filtration,²⁰ microfiltration,^{21–23} deterministic lateral displacement (DLD),^{24,25} pinched flow fractionation,²⁶ hydrophoretic filtration,²⁷ and field-flow fractionation (FFF)²⁸ have been employed to sort blood cells without complex apparatus, but typically high-throughput operation is not available, and systems often require sheath fluids for higher efficiency.

Another recent emerging passive blood cell sorting approach based on hydrodynamics utilizes fluid inertia in microchannels.²⁹ Commonly, inertia is ignored since the associated Reynolds number (Re : the dimensionless ratio of inertial force to viscous force) is small due to the small channel scale and low flow velocity, although moderate Reynolds number flows ($Re = 10–100$) frequently occur in microchannels. It should be highlighted that inertia-based approaches fundamentally offer simple, precise and high-throughput features, making them great candidates for highly efficient cell manipulation. There are two main inertial effects: inertial particle focusing (or migration) and secondary flow.²⁹ Briefly, microparticles flowing in straight microchannels experience a net inertial lift force, laterally migrating particles to ~ 0.6 times the channel half length.^{29–32} Since the lift force scales as $F_L \propto \rho U^2 a^4 / H^2$ (where F_L is the lift force, U is the flow velocity, a is the particle diameter, and H is the microchannel dimension),²⁹ particles with different sizes possess different lateral equilibrium positions. This unique size based particle self-aligning characteristic (inertial particle focusing) has been used for blood and other cell separation in straight channels;^{33,34} however, it should be noted that the lateral position difference between two differently sized cells/particles is subtle. Therefore, sorting cells in straight microchannels *via* fluid inertia still remains a challenge (low purity and efficiency).

In order to create distinct lateral cell and particle focusing profiles, secondary flows, transverse fluid motion to the primary flow, have been used.^{6,35–38} Secondary flow arises when the channel curvatures vary (*e.g.*, spiral^{6,36,38,39} or curving^{35,40} channels), and Dean flow²⁹ is the well-known lateral flow motion in curved channels. Lateral flow motion modifies the original inertial particle focusing profile in straight channels. Thus, a balance between Dean flow (*i.e.*, drag) and inertial lift force creates new and distinct focusing profiles, enabling highly efficient blood cell separation in straight channels. Dean flow-based blood separation showed great potential for effective blood cell separation, but note that the microparticle focusing quality decreases when the particle concentration becomes high. This is due to particle–particle interactions⁴¹ preventing a large portion of particles from migrating to their equilibrium positions. To resolve this issue, diluted

blood samples have been used, though the dilution process consequently lowers the cell count based throughput (note that still the volumetric processing rate is high). Therefore, to achieve higher cell processing rates, parallelization is essential, but for spiral^{6,36,38,39} or curving^{35,40} channels, it is difficult to implement due to their large two dimensional channel layouts.

In this work, we present a novel inertial platform for high-throughput, precise and sheathless particle and blood cell separation in straight channels with microstructures. Note that using a straight channel is an important feature because it allows for massive parallelization for extremely high throughput.^{33,42} For the presented new inertial sorter, we strategically add microstructures within straight microchannels to induce localized secondary flows^{43–45} which modify the original particle and cell focusing profiles in straight rectangle channels. It is important to mention that the microstructure induced secondary flow should be differentiated from Dean flow. Dean flow inherently perturbs the entire flow field, but microstructure based secondary flow creates localized vortices where higher flow controllability can be anticipated.⁴⁶ The overall channel design is presented in Fig. 1. The channel consists of three sections: (1) a straight low-aspect-ratio rectangular channel, (2) a straight channel with a series of symmetrically positioned square microstructures and (3) a trifurcating outlet. In short, when a mixture of two different-sized particles is introduced, each particle's position is determined by a competition between inertial lift force and microstructure induced secondary flow. After passing section (1) and (2), large particles migrate to the middle of the channel while small particle streams are located at the channel sidewalls (see Fig. 1A(iv)) where particles can exit to the desired outlets (section (3)) based upon their sizes. We successfully demonstrated the separation of 5.5 and 9.9 μm particles with high separation efficiencies ($>92\%$ and 98% , respectively) and purities ($>98\%$ and 92% , respectively) with a throughput of approximately 310 and 290 particles per second, respectively (in the case of a single channel). The present device is then applied to separate RBCs and WBCs. Diluted blood was fractionized with an efficiency of 89.7% and a purity of 91.0% for WBCs, and 99.8% and 99.6% for RBCs, respectively. The device can process diluted blood with a throughput of 10.8 mL min^{-1} when parallelized. We discuss the comprehensive numerical and experimental studies of the particle separation mechanism, the characterization of secondary flow motion, and the particle migration behaviours and quality of various sizes of microparticles and human blood.

Results and discussion

Design and operating mechanism of the inertial separator

A CAD layout of the microchannel used for particle/cell separation is presented in Fig. S1.† The inertial separation platform presented consists of a straight rectangular channel section (width (W) $120 \mu\text{m}$ \times height (H) $21 \mu\text{m}$ \times length (L) 2.5 cm)

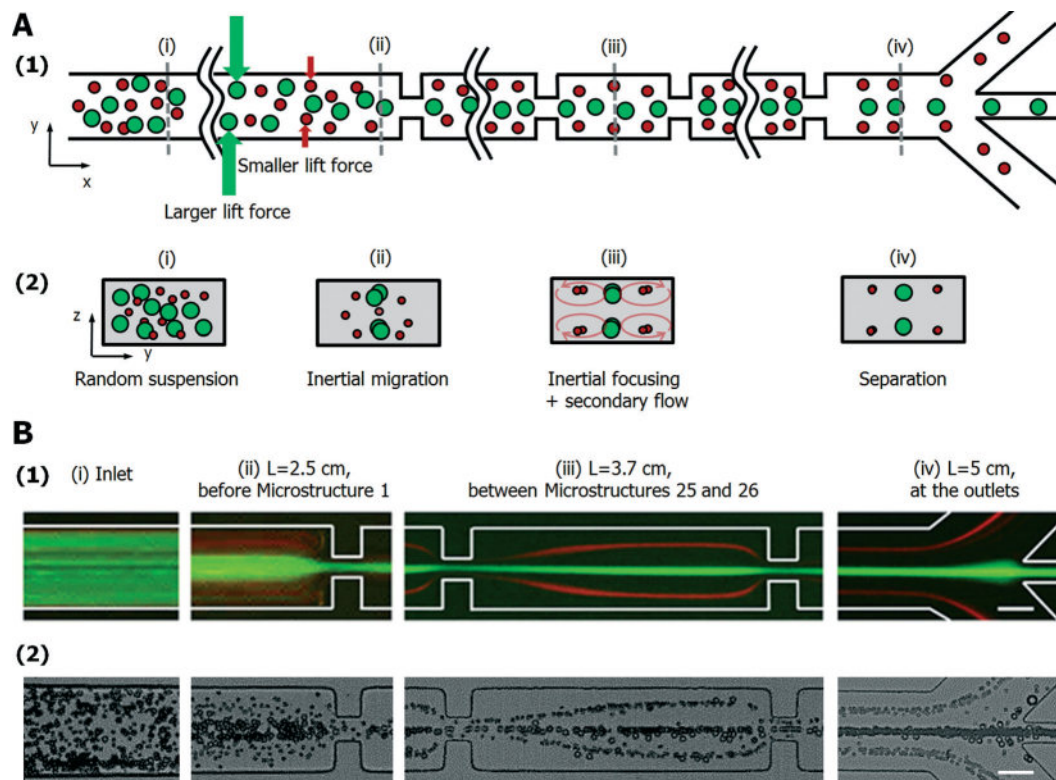


Fig. 1 Design and operating principles of the inertial particle separator. A. (1–2) Schematics of the inertial particle and cell separator (not to scale). Randomly incoming mixed microparticles (i) are separated through a three-step process: (ii) first, large particles (green) vertically focus at the centre of the channel, while no distinct focusing was shown for small particles (red). (iii) Microstructures induce secondary flow, migrating small particles near channel sidewalls, while the large particles remain focused in the channel centre. (iv) Each particle stream exits to the desired outlets. B. Experimental results demonstrating the inertial particle separation of a mixture of 5.5 and 9.9 μm polystyrene microspheres. (1) and (2) represent the fluorescence images and minimum light intensity image stacks, respectively. All scale bars represent 50 μm .

followed by a section containing 40 pairs of square microstructures (side length (S) 45 $\mu\text{m} \times H$ 21 μm with a spacing of 500 μm and a total length of 2 cm) symmetrically located on the side walls. Lastly, there is a straight rectangular channel section (W 120 $\mu\text{m} \times H$ 21 $\mu\text{m} \times L$ 0.5 cm) before a trifurcating outlet section (widths of 125, 30 and 125 μm with a height of 21 μm), all of which are outlined in Fig. 1A. For easier sorted sample handling, the two symmetrical side branch outlets re-join together into a single outlet (see Fig. S1[†]).

Mixed particles and cells are injected through a single inlet without sheath fluids. As the mixed microparticles travel downstream in the straight section, each particle experiences inertial lift forces. Large particles (green in Fig. 1A) experience considerable lift forces that allow them to migrate close to the channel centre when a low aspect ratio of the channel is used (see Fig. 1A(ii)). For small particles, owing to smaller lift forces, no obvious focusing profile was found, but particles were positioned close to the channel centre. Focusing large particles at the two equilibrium positions in the channel centre ahead of the microstructure zone is an important pre-step since interactions between particles and secondary flows occurring in the microstructure zone can be better controlled by minimizing particle–particle interactions. Next, all particles enter the microstructure zone. Optimal microstructure

design parameters and operating conditions were determined by detailed numerical analysis, which are all described in the “Numerical characterization of microstructure-induced secondary flows and particle migration” section below. Microstructures induce two localized pairs of helical vortices that mainly alter the motion of small particles (*i.e.*, the secondary flow effect is stronger than the inertial lift forces), creating new small particle focusing profiles near the sidewalls of the channel (Fig. 1A(iii)). Note that for large particles, since the inertial lift forces still remain dominant over the secondary flow, they remain in the middle of the channel when they travel through the microstructure zone.

After passing the microstructure zone, small particles are positioned close to the channel sidewall, and large particles are located in the channel centre. Then they enter the last straight rectangular channel before the trifurcating outlet. This section stabilizes the interactions between lift force and secondary flow, facilitating the two different sized particles to exit to the desired outlets, as shown in Fig. 1A(iv). Particle mixture separation stages along the channel are presented in Fig. 1B. A mixed solution of 5.5 μm (red) and 9.9 μm (green) polystyrene beads was injected at a Reynolds number of 35.5 (or an equivalent flow rate of 150 $\mu\text{L min}^{-1}$). Image stacks of 400 fluorescence images and corresponding minimum light

intensity plots from 2000 high speed images at different channel locations are presented in Fig. 1B(1) and (2), respectively, and continuous particle mixture separation is presented in Movie S1.† As can be seen, passive, efficient and high quality microparticle separation is clearly demonstrated solely by fluid inertia.

The presented methods should be distinguished from other particle separation approaches reported previously. First, with regard to Dean flow based separation,^{6,36,39,47,48} both approaches share much in common with manipulating inertia *via* the channel structure, though microstructure induced secondary flows are more localized where a large controllability is expected. Furthermore, parallelization using straight channels is better suited than large spatial spiral designs. Compared with other blood separation methods by Warkiani *et al.*⁴⁹ and Bhagat *et al.*,⁵⁰ our approach may look similar, but they are fundamentally different because they utilized pinched flow,²⁶ not microstructure induced secondary flow. Also note that the focusing mechanism in the present design is intrinsically dissimilar from that of the method proposed by Park *et al.*⁵¹ A seemingly analogous channel design was used, but both the channel dimension and the resulting operating mechanism are completely different. Park

*et al.*⁵¹ exploited vortices trapped in expansion regions rotating with an axis orthogonal to the primary flow direction which pinch particles for separation. However, the vortices in this work expand throughout the channel, traveling downstream as helical motions with the rotating axis parallel to the main flow direction.

Numerical characterization of microstructure-induced secondary flows and particle migration

Local helical vortices (*i.e.*, secondary flow) are created by strategically adding microstructures within the channel. While large particles are not greatly affected by secondary flow because of large inertial lift forces, small particle trajectories are mainly determined by secondary flow. In order to understand the secondary flow motion and particle behaviours more in depth, we conducted two separate sets of simulations: (1) flow field without particles using the finite element method (FEM) and (2) flow field with microparticles using the lattice Boltzmann method (LBM).^{52–55}

We first investigated the secondary flow from local microstructures without particles. Three-dimensional models of microchannels with multiple microstructures were constructed and analysed using COMSOL Multiphysics. Briefly, we solved

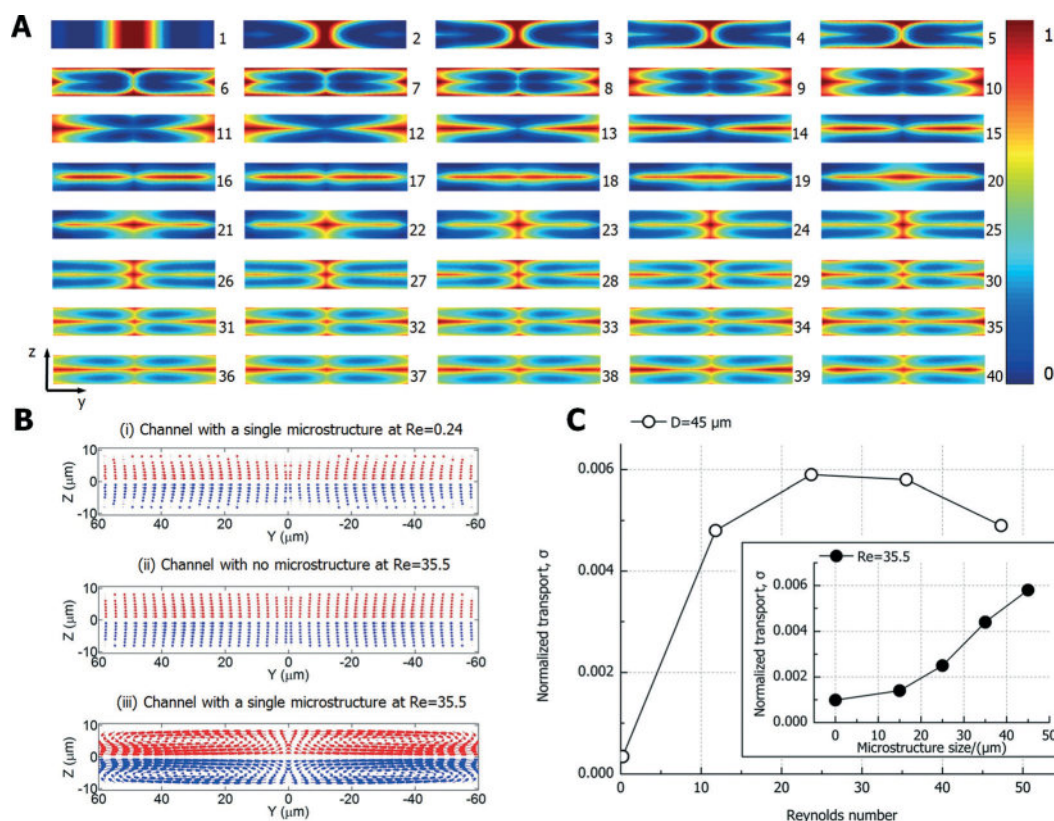


Fig. 2 Numerical analysis of secondary flows in the inertial separator. A. Two dimensional cross-section views of the convection–diffusion solutions simulated for 40 microstructures, presenting the evolution of the secondary flow. Blue and red represents normalized concentrations between 0 and 1. B. Vector plots of net lateral velocity for (i) Stokes flow in a channel with a single microstructure, (ii) inertial flows in a straight channel with no microstructure and (iii) inertial flows in a channel with a single microstructure. C. Normalized transport (σ , maximum net lateral velocity in YZ-plane divided by the free-stream velocity) is plotted as a function of Reynolds number, as well as the microstructure size (inset) at $Re = 35.5$.

the full Navier–Stokes (NS) equations and then solved the convection–diffusion equations from the velocity fields obtained from NS solutions. Fig. 2A shows a two-dimensional cross-section evolution as a function of microstructure number. The purpose is to identify how the secondary flow behaves with increasing number of microstructures, determining how many microstructures are required to reach a steady state. Due to the channel symmetry, two pairs of vortices are formed, and more secondary effects add on upon passing more microstructures, as shown in Fig. 2A. It should be noted that after passing the 30th microstructure, little flow motion change was added, even with additional microstructures, and this characteristic agrees well with our experimental results presented in the following sections.

We also simulated a single pair of microstructures at a moderate Reynolds number ($Re = 35.5$). For our controls, two cases of Stokes flow (*e.g.*, $Re \approx 0$) and inertial flow without microstructures were also studied. We compared them using net lateral velocity vectors as shown in Fig. 2B. As expected, no significant secondary flows were presented for Stokes flow and inertial flow without microstructures, although a clear net secondary motion of two pairs of vortices is presented for inertial flow with microstructures (see Fig. 2B(iii)). All of these indicate that only interactions between the microstructure and fluid inertia can create secondary flows. To characterize the degree of secondary flow intensity for various flow and system conditions, the normalized transport^{43,56} (σ) was calculated and plotted in Fig. 2C. The normalized transport is a useful parameter to quantify the net secondary flow motion, and as can be seen in Fig. 2C, the magnitude of σ increases gradually as the Reynolds number becomes large. This indicates an increase of inertial effects, but these effects then decrease beyond $Re = 23.7$. This trend of variation in the magnitude of σ is predicted, indicating a change in the mode of the secondary flow.⁴⁶ The dependence of normalized transport on microstructure size (side length) was also investigated at $Re = 35.5$ (see Fig. 2C inset). As the microstructure size increases, stronger secondary flows were presented. This can be explained when the fluid passes around a large microstructure, a large transverse pressure gradient is generated for stronger inertial secondary flows. Thus, Reynolds number and microstructure size can be used independently to tune and control the intensity of the net secondary flow to precisely manipulate particles. In this study, to maximize the inertial effect, $45 \mu\text{m}$ square microstructures were used while fixing a gap of $30 \mu\text{m}$ between microstructures in order to prevent any potential clogging issues.

It is worthwhile to mention the microstructure spacing effect. The spacing between two adjacent microstructures in the main stream direction is another key parameter for determination of microstructure induced secondary flow. Our previous study⁴³ showed that shorter spacing conditions yielded less predictable flow deformations due to non-linear superposition of secondary flows. Amini *et al.*⁴⁶ reported that for 3–4 times of the structure dimension, the secondary flow effect saturates; therefore, the spacing was set to $500 \mu\text{m}$ (10 times

the length of the square microstructures), ensuring linear secondary flow superposition.

As our second simulation set, we also numerically investigated particle-laden flows. We employed the lattice-Boltzmann method (LBM)^{52–55} over FEM to simulate particle–fluid/particle–particle interactions. Compared with FEM, the LBM utilizes a fixed Cartesian grid to model moving solid particles, allowing parallel computing⁵² for efficient three-dimensional simulations with multiple microparticles. The details of simulation can be found elsewhere,^{54,55} but the method is based on the microscopic models and mesoscopic kinetic equation⁵² to model particle suspensions.⁵³ Briefly, we applied a second order interpolation based curved boundary treatment⁵⁷ on the solid boundaries to accurately capture the particle surface. A corrected momentum exchange method⁵⁴ was employed to calculate the hydraulic force acting on the particles. Previous numerical studies⁵⁴ showed good agreement between LBM and FEM with high computational efficiency, validating our approach. Our simulations were performed in a domain with $40 \times 240 \times 1024$ lattice nodes (equivalent to $H: 20 \times W: 120 \times L: 512 \mu\text{m}$) containing a complete periodic section of a channel with one pair of microstructures ($S: 45 \times 45 \mu\text{m}$ squares on each side). Note that all simulations were conducted at $Re = 35.5$ with periodic boundary conditions.

We first investigated single-sized large particle ($9.9 \mu\text{m}$) behaviours, and four representative particle migration trajectories are presented in Fig. 3A (green colour scheme). Large microparticles were mainly found in the channel centre before entering the microstructure zone, and after passing several microstructures, they quickly focused in the channel centre (see Movie S2†). Four small particle ($5.5 \mu\text{m}$) trajectories are also presented in Fig. 3B (red colour scheme). As opposed to large beads, small particles did not migrate to the channel centre as they migrated downstream but exhibited stable trajectories close to the channel sidewalls due to the interactions with the helical secondary flows (see Movie S3†). We found that small particle motions strongly depend on their initial positions and particle–particle interactions (see Fig. S2†). When the particle–particle interaction is negligible, each particle's final path is determined by the secondary flow with stable trajectories close to sidewalls; however, if there is crosstalk between particles, altered trajectories were seen immediately after the interaction. For example, in Fig. 3B(4) at $X \approx 29 \mu\text{m}$, one of the particle trajectories (coloured in pink) is modified because of the other particle, though soon it was stabilized back (see Fig. S3†). We also found that sometimes this particle–particle interaction could push a particle initially positioned in the channel centre towards the channel sidewall (see Fig. S4†). Small particles positioned near the channel centre find it difficult to move towards the side wall by themselves since the channel centre is where particles experience the weakest secondary flows but the strongest inertial lift forces.

Along with single-sized particle simulations, we numerically predicted particle motions of a mixed sample with two $9.9 \mu\text{m}$ and two $5.5 \mu\text{m}$ microspheres. As presented in Fig. 3C

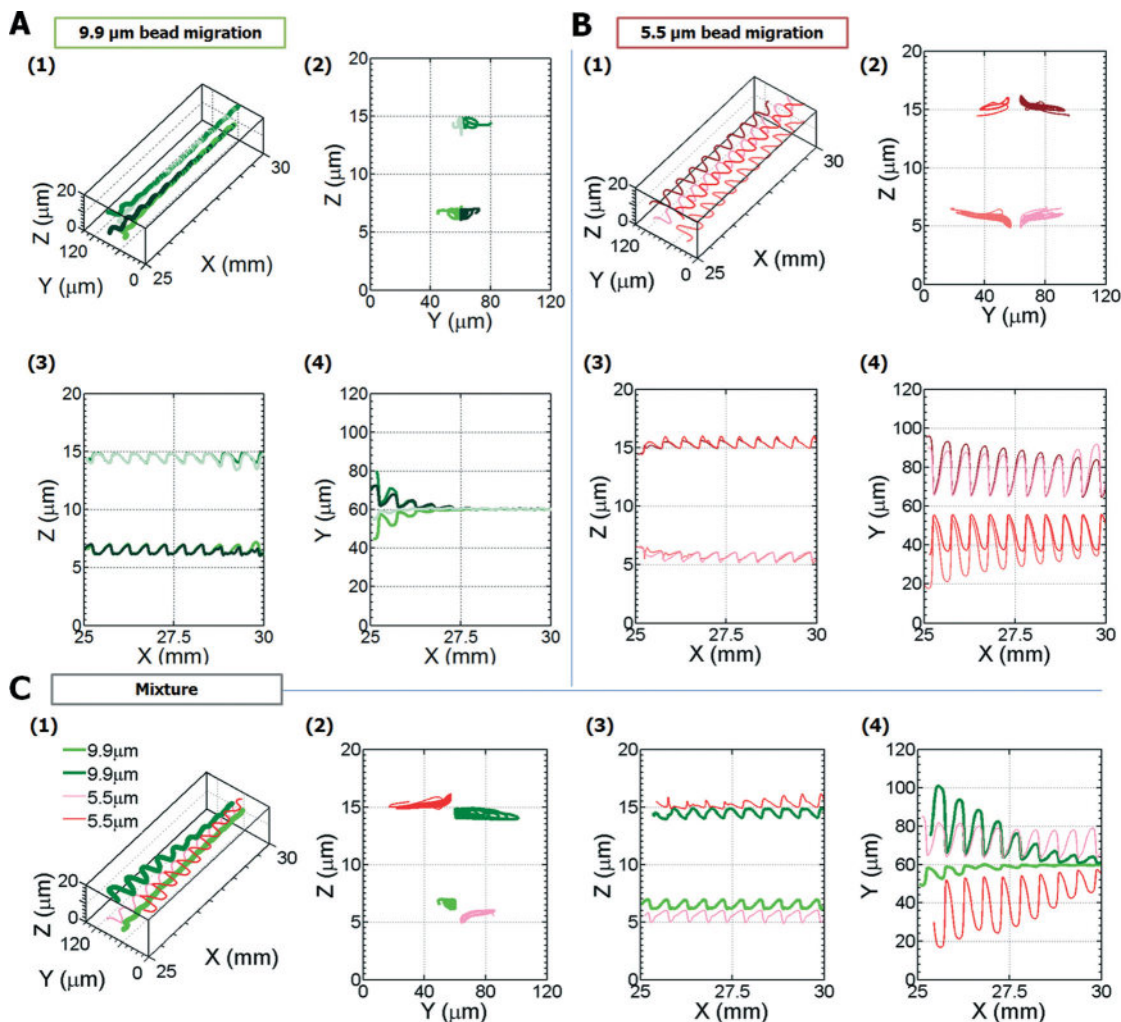


Fig. 3 (Colour on-line) Numerical analysis of particle behaviours in the inertial separator. A. Four representative $9.9\ \mu\text{m}$ polystyrene microsphere trajectories traveling in water. As microspheres migrate downstream, they focus in the channel centre. B. Trajectories of four $5.5\ \mu\text{m}$ polystyrene beads in different coordinates. Particles migrate towards channel walls due to the secondary flows. C. Microparticle migrations of a mixed sample (two 9.9 and $5.5\ \mu\text{m}$ polystyrene microspheres). As expected, $9.9\ \mu\text{m}$ polystyrene microspheres position in the centre and the $5.5\ \mu\text{m}$ ones remain close to the channel walls.

and Movie S4[†] large particles (green colour scheme) migrated to the channel centre which agrees well with our experimental observations. Compared to the single-sized particle case, there was a delay in large particle (coloured green in Fig. 3C(4)) migration to the centre, which can be explained by the particle's initial position. Small particles (red colour scheme) showed a similar trend to the single-sized case, but their trajectories are relatively unstable. This can be attributed to the fact that small particles are prone to be influenced by large particles particularly at the bottleneck regions (*i.e.*, between microstructures). We plotted the mixed particle trajectories further downstream in Fig. S5[†] and confirmed that large particles were still positioned in the centre and small particles remain close to the channel side walls.

Single-sized particle migration characterization

Particles with various sizes and flow rates were experimentally tested to identify and characterize the particle

behaviours in our inertial separator. Particle concentrations were 0.002% and 0.01% (w/w) for particle sizes $\leq 6.8\ \mu\text{m}$ and $\geq 7.9\ \mu\text{m}$, respectively. The minimum light intensity plots of 2000 image stacks for particles with various sizes before entering the outlets are presented in Fig. 4A. All particle behaviours can be accounted for by a balance of inertial lift force (*i.e.*, inertial particle migration) and secondary flow from microstructures. As can be seen in Fig. 4A, all particles at $\text{Re} = 0.24$ were distributed throughout the channel because of negligible inertial lift forces and secondary flows. However, as Reynolds number increases, particles smaller than $6.8\ \mu\text{m}$ were found close to the channel walls due to substantial secondary flow effects over inertial lift forces. For larger particles ($\geq 9.9\ \mu\text{m}$), when Re becomes larger than 11.8, inertial lift forces become dominant over the secondary flow effect, allowing the particles to migrate to the centre of the channel. For particles with sizes of $7.9\ \mu\text{m}$, an intermediate state was noticed where both inertial effects are compatible; therefore,

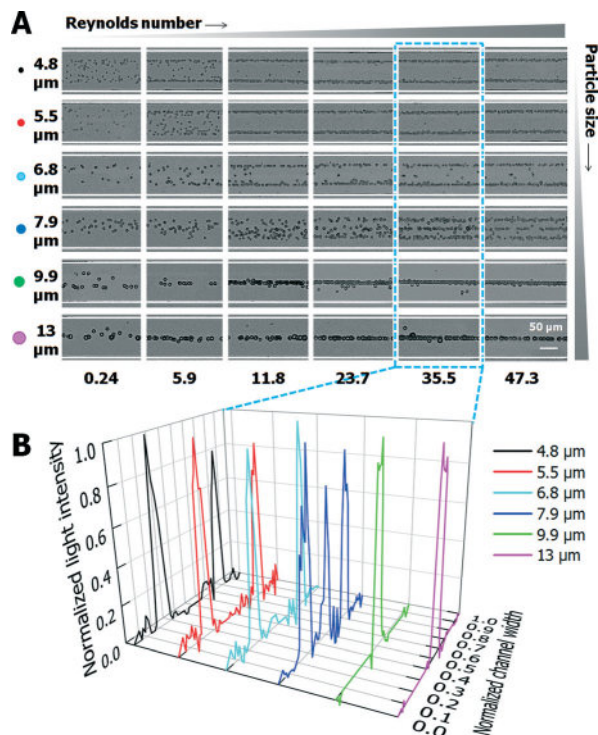


Fig. 4 Experimental characterization of particle migration under different sizes and flow conditions. A. Image stacks of different-sized particles at 5.0 cm (close to outlet). B. Normalized light intensity across the channel width of A at $Re = 35.5$.

particles were found in both the channel centre and side walls.

To quantitatively analyse the equilibrium positions of each particle size in the inertial separator, the normalized light intensity from Fig. 4A at $Re = 35.5$ across the channel width is processed and plotted in Fig. 4B and S6.† As the particle size increases, the equilibrium positions change from the channel sidewalls to the centreline. This indicates that as particle size becomes larger, inertial lift forces increase, accounting for the transition from the secondary flow governing regime to the inertial lift force regime. Note that a nearly identical trend was shown for Reynolds number of 47.3 as well (see Fig. 6A and B). Based on the particle behaviours, particle mixtures of sizes $\leq 6.8 \mu\text{m}$ and $\geq 9.9 \mu\text{m}$ can be potentially separated effectively at $Re = 35.5$ or 47.3.

Size-based microparticle separation

A mixture of microparticles with diameters of 5.5 and 9.9 μm was first tested to demonstrate particle separation. The tested particle concentrations were 0.001% and 0.01% (w/w) for 5.5 and 9.9 μm particles, respectively (concentration effects are separately discussed below). The mixture was injected through a single inlet, and Fig. 5A shows particle behaviours using the standard deviation plots⁴⁴ from 2000 image stacks at different downstream locations at $Re = 35.5$.

Particles randomly enter the channel inlet, but after passing the upstream straight section, large particles (9.9 μm)

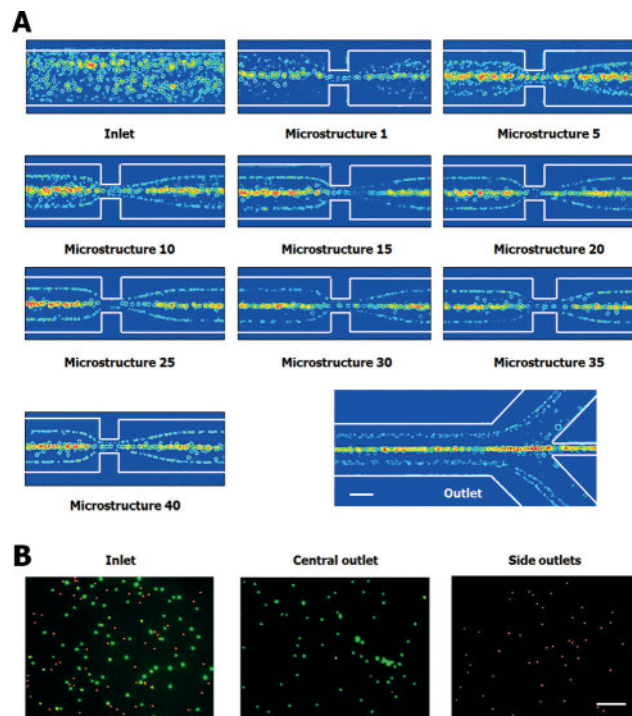


Fig. 5 Demonstration of 5.5 and 9.9 μm polystyrene microparticle separation. A. Standard deviation plots from 2000 image stacks qualitatively describing the successful size-based separation at $Re = 35.5$. B. Fluorescence images of particles collected from the inlet and two outlets. Green and red colours represent 9.9 and 5.5 μm particles, respectively. Scale bars represent 50 μm for A and 100 μm for B.

were mainly found in the centreline of the channel by fluid inertia. For small particles, they still remain unfocused, but due to the non-zero lift force acting on them, a large portion of small particles are found near the channel centre region as shown in Fig. 5A-Microstructure 1. Then, all particles enter the microstructure zone where helical secondary flows position small particles close to the channel sidewalls. As mentioned before, large particles will position in the channel centre without being affected by secondary flow, showing good agreement with the single-sized test (Fig. 4) and numerical prediction (Fig. 3A). Note that large particles obtain improved focusing characteristics as they pass a longer distance as predicted in the numerical analysis because a longer channel length is beneficial for narrow focusing.²⁹ These unique size-based particle migration behaviours create three distinct particle focusing profiles: one large particle centre stream and two small particle streams on each side. Based on these three particle streams, a three-branch outlet was designed which enables high quality particle sorting. Identical particle behaviours can also be seen from fluorescence imaging as shown in Fig. S7 and S8.† Fluorescence images of collected microspheres from each outlet and inlet are presented in Fig. 5B, confirming the particle separation.

The quality of particle separation is strongly affected by the particle concentration. We evaluated the separation quality by calculating the particle purity (the ratio of the number

of collected target particles to the number of collected total particles) and particle separation efficiency (the ratio of the number of collected target particles to the number of input target particles) based on flow and particle concentration conditions. The overall results are presented in Fig. 6. Among various tests (Fig. 6C and D), concentrations of 0.001% (w/w) and 0.01% (w/w) for 5.5 and 9.9 μm particles, respectively, were chosen for the baseline tests. Higher particle concentrations were also tested, though sorting purity and efficiency degraded because of the unwanted particle–particle interactions.⁴¹ For higher concentration mixtures, many small particles were found in the channel centre, as shown in Fig. S9.† This can be partially explained by the fact that large particles trigger small particles to be positioned at the channel centre instead of following the helical vortices which position particles on channel sidewalls. Note that the initial particle purity denoted in Fig. 6A stands for the fraction of each sized particle to the total number of particles before separation. All purity and efficiency quantities were processed using ImageJ (<http://rsb.info.nih.gov/ij/>). As a negative control (denoted as ‘Control’ in Fig. 6A and B), a straight channel without microstructures was tested. Flow rates of 1, 50, 100, 150 and 200

$\mu\text{L min}^{-1}$, encompassing Stokes and inertial regimes, were selected to characterize and evaluate the separation purity and efficiency. For Stokes flow ($Re = 0.24$), as expected, low quality separation and purity were shown (see Fig. 6A and B). For inertial flow, a flow rate of 150 $\mu\text{L min}^{-1}$ ($Re = 35.5$) yields the best separation results, and under this condition, a sorting efficiency of 98.3% and a purity of 92.3% were calculated for 9.9 μm particles (centre outlet). For 5.5 μm particles, an efficiency of 92.8% and a purity of 98.4% were calculated (side outlets). The throughput at this flow rate is about 310 and 290 particles per second for 5.5 μm and 9.9 μm particles, respectively, when a single channel is used.

Human blood cell separation

In the previous section, we successfully demonstrated 5.5 and 9.9 μm microsphere separation, and our platform can be used for RBC and WBC separation considering a good size overlap. For blood separation tests, we used diluted human blood samples in order to minimize the particle–particle interaction which degrades the particle focusing quality. In this work, concentrations of 0.25–0.5% of whole blood

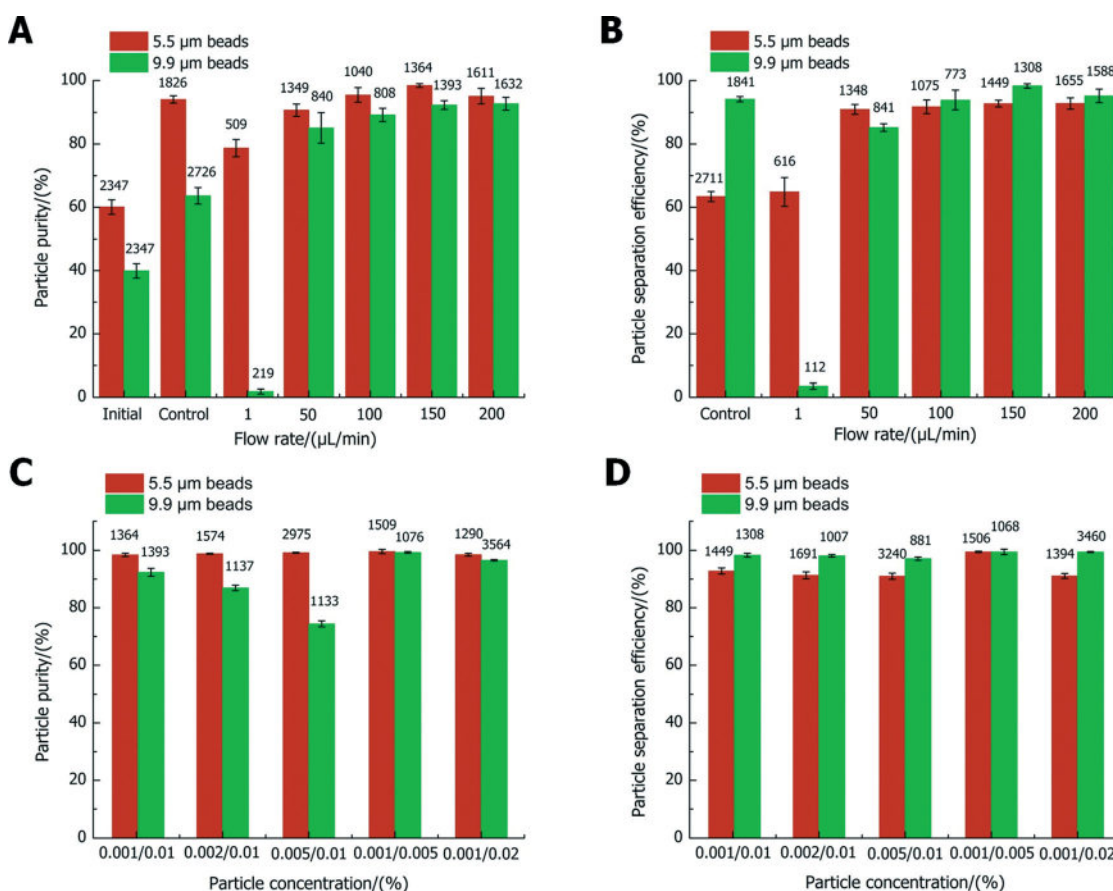


Fig. 6 Quantitative characterization of 5.5 and 9.9 μm polystyrene particle separation. A. Particle separation purity with fixed particle concentrations from the central and side outlets under various flow conditions. B. Particle separation efficiency for fixed particle concentrations under different flow rates. C. Separation purity of particles from the central and side outlets under different particle concentration conditions with a fixed flow rate of 150 $\mu\text{L min}^{-1}$. D. Separation efficiency for particles under different particle concentration conditions with a fixed flow rate of 150 $\mu\text{L min}^{-1}$. Each error bar represents the standard deviation of three independent measurements.

similar to other inertial microfluidic systems^{6,33,50} were used. Fig. 7A illustrates a schematic of RBC (red) and WBC (purple) sorting using our inertial platform. Analogous to microsphere sorting, large WBCs experience stronger inertial lift forces, thus they were found in the centreline of the channel, exiting through the central outlet. Small RBCs follow the secondary flows exerted by microstructures where they migrate to the channel sidewalls, exiting the side outlets. Using the inertial separator at $Re = 35.5$, the tested blood was well fractionized, as presented in Fig. 7B (see Movie S5†). Qualitative cell passes were presented using standard deviation plots from 2000 image stacks in Fig. 7C. Due to scarcity of WBCs compared to RBCs, a weaker trace of WBCs was shown in the centre outlet, though it can be seen that highly concentrated RBCs leave towards the side outlets.

Purity and separation efficiency in the case of 0.25% diluted RBCs and WBCs from the corresponding outlets were calculated and plotted in Fig. 7D under various flow conditions. A control channel (no microstructures) was also tested, and the corresponding results were included as well. Since RBCs are the majority of the blood constituents, the purity of RBCs was high even for the control and Stokes ($Re = 0.24$) flow, but the separation efficiencies were low as expected. In inertial flow, a flow rate of $150 \mu\text{L min}^{-1}$ ($Re = 35.5$), the

purities reach as high as 99.6% and 91.0% for RBCs and WBCs, respectively. The equivalent separation efficiencies are approximately 99.8% and 89.7% for RBCs and WBCs, respectively, demonstrating efficient blood separation. The throughput is over 1.3×10^4 RBCs per second under this condition.

For higher throughput, 0.5% diluted blood was tested, and the separation results of RBCs and WBCs are presented in Fig. S10.† As the concentration increases, the separation performance deteriorates, similar to the microsphere results. Though the separation performance of RBCs remains high, the purity of WBCs is reduced to 84.3% at a flow rate of $100 \mu\text{L min}^{-1}$, and the corresponding separation efficiency is 77.9%. However, the throughput can be as high as 2.5×10^4 RBCs per second in this case.

To move towards higher throughput, the device can deal with a higher hematocrit level sample, be operated at a higher flow rate or be massively parallelized.³³ Channel parallelization is chosen for this study because as mentioned above, samples with a higher concentration will reduce the sorting efficiency, and due to PDMS-glass delamination failure, the maximum flow rate was set. It should be noted that by using rigid channels made of Thermoset Polyester (TPE), Polyurethane Methacrylate (PUMA) and Norland Adhesive 81 (NOA81),⁵⁸ potentially a higher throughput can be attained.

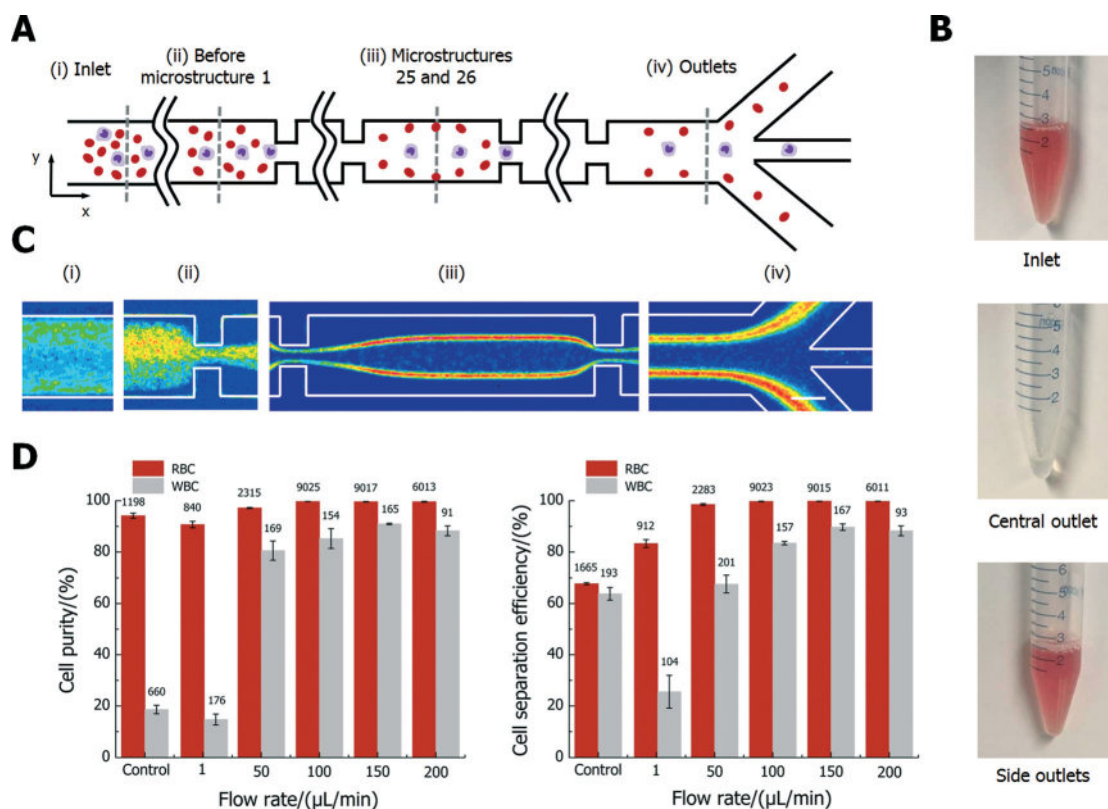


Fig. 7 Characterization of RBC and WBC separation from 0.25% (v/v) diluted human whole blood through our device. **A.** A schematic illustration of the separation process of RBCs and WBCs in the inertial microchannel. **B.** Representative results for before processing and showing successful separation. **C.** Standard deviation plots from 2000 image stacks qualitatively describing the separation of RBCs and WBCs (at $Re = 35.5$). Scale bar represents $50 \mu\text{m}$. **D.** Purity and separation efficiency of RBCs and WBCs collected from two outlets under various flow conditions. Each error bar represents the standard deviation of three independent measurements.

We determined that the present device can be arrayed with 72 radially arranged channels with a single inlet and two ring outlets which can process large volumes of blood continuously (see Fig. S11†). By calculation, when 0.25% diluted blood is tested at $Re = 35.5$, volumes of 10.8 mL min^{-1} can be processed. Moreover, with a channel stacking process⁵⁹ even higher throughput can be anticipated. This parallelization process will enable faster blood fractionation, processing large volumes of fluids.

Conclusions

In summary, in this work we present an inertial particle and cell separator using microstructure induced secondary flows. A balance of two inertial effects – inertial lift force and microstructure induced secondary flows – allows for precise alignments of different-sized microparticles and human blood cells at different lateral equilibrium positions in the channel. We successfully separate microspheres with two different size populations, and RBCs and WBCs from diluted human blood. High separation efficiency and purity were achieved for both bead and blood cases. Our device shows a great possibility to be massively paralleled to process 0.25% diluted whole blood with a throughput of 10.8 mL min^{-1} . In addition to separating RBCs and WBCs, the sorting principle presented here can be used for other cell separations. By utilizing the cell size difference between circulating tumor cells (CTCs) and blood cells, it is potentially possible to enrich CTCs from blood.

Materials and methods

Microchannel fabrication

Microchannels were fabricated by standard single layer photolithography using SU-8 2025 and polydimethylsiloxane (PDMS, Sylgard 184, Dow Corning, MI, USA) replica moulding protocols.

Microparticle and cell injection and imaging

Solutions with microspheres and human blood cells were injected using a syringe pump (Harvard Apparatus, MA, USA) operated between the range of $1 \text{ } \mu\text{L min}^{-1}$ and $400 \text{ } \mu\text{L min}^{-1}$. Microparticle migration was recorded using a high-speed camera (Vision Research, NJ, USA) mounted on an inverted microscope (Zeiss Axio Observer, Germany). Recorded image stacks were analysed and processed using ImageJ (<http://rsb.info.nih.gov/ij/>).

Microparticle specifications

4.8, 5.5, 6.8, 7.9, 9.9 and $13 \text{ } \mu\text{m}$ particle suspensions with coefficients of variation (CV) of 5%, 2%, 5%, 20%, 5% and 16%, respectively, were used for this study. All microparticles were purchased from Thermo Fisher Scientific PA, USA, except for $5.5 \text{ } \mu\text{m}$ microspheres which were from Polysciences, PA, USA, and $6.8 \text{ } \mu\text{m}$ particles from Spherotech, PA, USA. In order to prevent potential clogging, $40 \text{ } \mu\text{m}$ cell strainers

(Thermo Fisher Scientific, PA, USA) were used to filter dusts in the solutions before injection.

Standard deviation and minimum light intensity plots

Particle distributions were presented using standard deviation and minimum light intensity plots. Each pixel's standard deviation was calculated from an image stack and plotted in a single image as previously reported.⁴⁴

Blood cell preparation

For experiments with blood samples, fresh human whole blood was collected from a healthy consenting donor and stored in a vial at room temperature. Blood samples were gently rocked back and forth before use and resuspended in phosphate buffered saline (PBS) with 0.25% and 0.5% (v/v) concentrations.

Acknowledgements

This work was partially supported by the National Science Foundation (NSF) under grant number NSF-IIA-1444104 and Rensselaer Polytechnic Institute (RPI). Z. W. would like to acknowledge the China Scholarship Council (CSC) for the Chinese Government Scholarship sponsoring his study at RPI, and thank Prof. Yihua Cao at Beihang University for his administrative support. M. W. would like to acknowledge support from NSF of China (No. 51176089) and Y. C. would like to acknowledge support from National Postdoc Foundation of China (No. 2014 M550716). Device fabrication for this work was performed in part at the Micro and Nano Fabrication Clean Room (MNCR) at RPI. The authors would like to thank Mr. Kevin Paulsen at RPI for helpful discussion, and all the members of the Bio-Optofluidics Laboratory at RPI for their technical support.

References

- 1 M. Toner and D. Irimia, *Annu. Rev. Biomed. Eng.*, 2005, 7, 77.
- 2 D. R. Gossett, W. M. Weaver, A. J. Mach, S. C. Hur, H. T. K. Tse, W. Lee, H. Amini and D. Di Carlo, *Anal. Bioanal. Chem.*, 2010, 397, 3249–3267.
- 3 N. Nivedita and I. Papautsky, *Biomicrofluidics*, 2013, 7, 054101.
- 4 V. Srinivasan, V. K. Pamula and R. B. Fair, *Lab Chip*, 2004, 4, 310–315.
- 5 A. A. S. Bhagat, H. Bow, H. W. Hou, S. J. Tan, J. Han and C. T. Lim, *Med. Biol. Eng. Comput.*, 2010, 48, 999–1014.
- 6 L. Wu, G. Guan, H. W. Hou, A. A. S. Bhagat and J. Han, *Anal. Chem.*, 2012, 84, 9324–9331.
- 7 H. M. Davey and D. B. Kell, *Microbiol. Rev.*, 1996, 60, 641–696.
- 8 A. Kumar and A. Bhardwaj, *Biomed. Mater.*, 2008, 3, 034008.
- 9 A. L. Givan, *Flow cytometry: first principles*, John Wiley & Sons, 2013.
- 10 M. E. Piyasena and S. W. Graves, *Lab Chip*, 2014, 14, 1044–1059.

- 11 S. Fukuda and G. W. Schmid-Schönbein, *J. Leukocyte Biol.*, 2002, **72**, 133–139.
- 12 G. M. Whitesides, *Nature*, 2006, **442**, 368–373.
- 13 M. L. Kovarik, P. C. Gach, D. M. Ornoff, Y. Wang, J. Balowski, L. Farrag and N. L. Allbritton, *Anal. Chem.*, 2011, **84**, 516–540.
- 14 S. Haeberle and R. Zengerle, *Lab Chip*, 2007, **7**, 1094–1110.
- 15 F. Petersson, A. Nilsson, C. Holm, H. Jonsson and T. Laurell, *Analyst*, 2004, **129**, 938–943.
- 16 J. Nam, H. Lim, D. Kim and S. Shin, *Lab Chip*, 2011, **11**, 3361–3364.
- 17 M. MacDonald, G. Spalding and K. Dholakia, *Nature*, 2003, **426**, 421–424.
- 18 M. S. Pommer, Y. Zhang, N. Keerthi, D. Chen, J. A. Thomson, C. D. Meinhardt and H. T. Soh, *Electrophoresis*, 2008, **29**, 1213–1218.
- 19 X.-B. Wang, J. Yang, Y. Huang, J. Vykoukal, F. F. Becker and P. R. Gascoyne, *Anal. Chem.*, 2000, **72**, 832–839.
- 20 M. Yamada and M. Seki, *Lab Chip*, 2005, **5**, 1233–1239.
- 21 T. A. Crowley and V. Pizziconi, *Lab Chip*, 2005, **5**, 922–929.
- 22 H. M. Ji, V. Samper, Y. Chen, C. K. Heng, T. M. Lim and L. Yobas, *Biomed. Microdevices*, 2008, **10**, 251–257.
- 23 X. Chen, C. C. Liu and H. Li, *Sens. Actuators, B*, 2008, **130**, 216–221.
- 24 L. R. Huang, E. C. Cox, R. H. Austin and J. C. Sturm, *Science*, 2004, **304**, 987–990.
- 25 S. H. Holm, J. P. Beech, M. P. Barrett and J. O. Tegenfeldt, *Lab Chip*, 2011, **11**, 1326–1332.
- 26 M. Yamada, M. Nakashima and M. Seki, *Anal. Chem.*, 2004, **76**, 5465–5471.
- 27 S. Choi, S. Song, C. Choi and J.-K. Park, *Lab Chip*, 2007, **7**, 1532–1538.
- 28 F. von der Kammer, S. Legros, T. Hofmann, E. H. Larsen and K. Loeschner, *TrAC, Trends Anal. Chem.*, 2011, **30**, 425–436.
- 29 D. Di Carlo, *Lab Chip*, 2009, **9**, 3038–3046.
- 30 J. Zhou, P. V. Giridhar, S. Kasper and I. Papautsky, *Lab Chip*, 2013, **13**, 1919–1929.
- 31 J. M. Martel and M. Toner, *Annu. Rev. Biomed. Eng.*, 2014, **16**, 371–396.
- 32 H. Amini, W. Lee and D. Di Carlo, *Lab Chip*, 2014, **14**, 2739–2761.
- 33 A. J. Mach and D. Di Carlo, *Biotechnol. Bioeng.*, 2010, **107**, 302–311.
- 34 M. Masaeli, E. Sollier, H. Amini, W. Mao, K. Camacho, N. Doshi, S. Mitragotri, A. Alexeev and D. Di Carlo, *Phys. Rev. X*, 2012, **2**, 031017.
- 35 D. Di Carlo, D. Irimia, R. G. Tompkins and M. Toner, *Proc. Natl. Acad. Sci. U. S. A.*, 2007, **104**, 18892–18897.
- 36 S. S. Kuntaegowdanahalli, A. A. S. Bhagat, G. Kumar and I. Papautsky, *Lab Chip*, 2009, **9**, 2973–2980.
- 37 J. Zhang, S. Yan, R. Sluyter, W. Li, G. Alici and N.-T. Nguyen, *Sci. Rep.*, 2014, **4**, 4527.
- 38 G. Guan, L. Wu, A. A. Bhagat, Z. Li, P. C. Chen, S. Chao, C. J. Ong and J. Han, *Sci. Rep.*, 2013, **3**, 1475.
- 39 W. C. Lee, A. A. S. Bhagat, S. Huang, K. J. Van Vliet, J. Han and C. T. Lim, *Lab Chip*, 2011, **11**, 1359–1367.
- 40 D. Di Carlo, J. F. Edd, D. Irimia, R. G. Tompkins and M. Toner, *Anal. Chem.*, 2008, **80**, 2204–2211.
- 41 W. Lee, H. Amini, H. A. Stone and D. Di Carlo, *Proc. Natl. Acad. Sci. U. S. A.*, 2010, **107**, 22413–22418.
- 42 S. C. Hur, H. T. K. Tse and D. Di Carlo, *Lab Chip*, 2010, **10**, 274–280.
- 43 A. J. Chung, D. Pulido, J. C. Oka, H. Amini, M. Masaeli and D. Di Carlo, *Lab Chip*, 2013, **13**, 2942–2949.
- 44 A. J. Chung, D. R. Gossett and D. Di Carlo, *Small*, 2013, **9**, 685–690.
- 45 K. S. Paulsen, D. Di Carlo and A. J. Chung, *Nat. Commun.*, 2015, **6**, 6976.
- 46 H. Amini, E. Sollier, M. Masaeli, Y. Xie, B. Ganapathysubramanian, H. A. Stone and D. Di Carlo, *Nat. Commun.*, 2013, **4**, 1826.
- 47 A. A. S. Bhagat, S. S. Kuntaegowdanahalli and I. Papautsky, *Lab Chip*, 2008, **8**, 1906–1914.
- 48 J. Seo, M. H. Lean and A. Kole, *Appl. Phys. Lett.*, 2007, **91**, 033901.
- 49 M. E. Warkiani, A. K. P. Tay, B. L. Khoo, X. Xiaofeng, J. Han and C. T. Lim, *Lab Chip*, 2015, **15**, 1101–1109.
- 50 A. A. S. Bhagat, H. W. Hou, L. D. Li, C. T. Lim and J. Han, *Lab Chip*, 2011, **11**, 1870–1878.
- 51 J.-S. Park, S.-H. Song and H.-I. Jung, *Lab Chip*, 2009, **9**, 939–948.
- 52 S. Chen and G. D. Doolen, *Annu. Rev. Fluid Mech.*, 1998, **30**, 329–364.
- 53 C. K. Aidun and J. R. Clausen, *Annu. Rev. Fluid Mech.*, 2010, **42**, 439–472.
- 54 Y. Chen, Q. Cai, Z. Xia, M. Wang and S. Chen, *Biophys. Rev.*, 2013, **88**, 013303.
- 55 Y. Chen, Q. Kang, Q. Cai, M. Wang and D. Zhang, *Commun. Comput. Phys.*, 2015, **18**, 757–786.
- 56 H. Amini, E. Sollier, W. M. Weaver and D. Di Carlo, *Proc. Natl. Acad. Sci. U. S. A.*, 2012, **109**, 11593–11598.
- 57 R. W. Mei, L. S. Luo and W. Shyy, *J. Comput. Phys.*, 1999, **155**, 307–330.
- 58 E. Sollier, C. Murray, P. Maoddi and D. Di Carlo, *Lab Chip*, 2011, **11**, 3752–3765.
- 59 M. E. Warkiani, B. L. Khoo, D. S.-W. Tan, A. A. S. Bhagat, W. T. Lim, Y. S. Yap, S. C. Lee, R. A. Soo, J. Han and C. T. Lim, *Analyst*, 2014, **139**, 3245–3255.